Journal of Wind Engineering & Industrial Aerodynamics 244 (2024) 105617

Contents lists available at ScienceDirect

Journal of Wind Engineering & Industrial Aerodynamics

journal homepage: www.elsevier.com/locate/jweia

Aerodynamic noise from a high-speed train bogie with complex geometry under a leading car

Yuan He [a,*], David Thompson [a], Zhiwei Hu [b]

[a] Institute of Sound and Vibration Research, University of Southampton, Southampton, SO17 1BJ, UK
[b] Aerodynamics & Flight Mechanics Research Group, University of Southampton, Southampton, SO17 1BJ, UK

ARTICLE INFO

Keywords:
Train bogie
Aerodynamic noise
Noise source
DDES
Ffowcs Williams & Hawkings

ABSTRACT

Among the various aerodynamic noise sources associated with high-speed trains, the bogie regions, and particularly the leading bogie, contribute most to the overall noise. To control this noise, insight into the noise generation mechanisms is imperative but relevant studies are limited due to the difficulties of simulating the flow in regions with complex geometry. An investigation is presented of the aerodynamic noise from a bogie under the leading car of a high-speed train using Delayed Detached Eddy Simulation method. A hybrid grid system is utilized to simulate the flow field, which provides input for the far-field noise calculations based on the Ffowcs Williams and Hawkings equation. Analysis shows that the outer bogie components experience large pressure fluctuations as they are immersed in the shear layer detached from upstream, which is therefore identified as playing a critical role in the noise generation. The resulting noise spectra are broadband and dominated by low frequencies. Compared with the bogie, the bogie cavity and train nose emit 5 dB greater sound power for the current geometry. This study improves understanding of the mechanisms behind the generation of aerodynamic noise in train bogies and lays the foundations for future studies of train bogie noise reduction.

1. Introduction

As the speeds of high-speed trains continue to rise, the associated aerodynamic problems become more significant. On the one hand, aerodynamic issues, such as the aerodynamic drag, energy consumption, slipstreams, ballast flight, and trains passing through tunnels draw more and more attention (Ricco et al., 2007; Baker, 2014; Bell et al., 2015; Jing et al., 2019; Tian, 2019; Guo et al., 2020). On the other hand, it becomes imperative to mitigate the environmental impacts due to aerodynamic noise (Thompson et al., 2015; Tian, 2019). The increase in running speed of trains results in a more rapid growth of aerodynamic noise compared to other sources such as rolling noise. Thompson et al. (2015) found that the aerodynamic noise becomes dominant when train speeds exceed approximately 350 km/h. Among the various aerodynamic noise source regions, such as the pantographs, gaps between coaches, and the wake region, the bogie regions make the most substantial contribution to the overall noise (Thompson et al., 2015). Although the pantographs may produce high noise peaks during the train pass-by, there are many more bogies than pantographs on a train, so the bogies dominate the overall pass-by noise (Thompson et al., 2015; Li et al., 2020; Liu et al., 2021). Furthermore, the leading bogie is identified as the one that not only produces the highest drag but also forms the strongest noise source compared with other bogies (Nagakura, 2006; Lauterbach et al., 2012; Guo et al., 2022). Therefore, to effectively manage the overall aerodynamic noise of high-speed trains, it is imperative to understand the noise generation mechanisms and the distinctive aerodynamic noise characteristics of bogies, particularly the leading one.

Experiments employing scaled models have previously been conducted to investigate the characteristics of aerodynamic noise produced by train bogies. Lauterbach et al. (2012) conducted experiments using a 1/25 scale train model in a cryogenic wind tunnel to investigate the dependence of aerodynamic noise generation on Reynolds number and Mach number. The noise generated by the leading bogie was found to be only weakly dependent on Reynolds number; the speed power law exponent was approximately equal to 6 over a wide range of Reynolds numbers. Latorre Iglesias et al. (2017) measured the aerodynamic noise from a 1/7 scale bogie mounted under a model train body in a wind tunnel, and found that the noise spectrum was dominated by low frequencies, which was also found by Lauterbach et al. (2012). Yamazaki et al. (2019) also conducted experiments using a 1/7 scale model. A two-dimensional microphone array, positioned at the trackside, was

* Corresponding author.
E-mail address: yh12n18@soton.ac.uk (Y. He).

https://doi.org/10.1016/j.jweia.2023.105617
Received 2 October 2023; Received in revised form 10 November 2023; Accepted 29 November 2023
Available online 8 December 2023

employed to measure the aerodynamic noise produced by various configurations of the bogie, situated within the cavity under the train model. The results showed that the wheelsets, as well as the motors and the brakes, have a significant impact on the bogie aerodynamic noise.

Although some experiments such as these have been conducted to investigate the bogie aerodynamic noise, the mechanisms responsible for its generation remain not fully comprehended. Therefore, it is necessary to adopt numerical methods to facilitate the understanding. For numerical simulations of aerodynamic noise in an industrial context, the most popular approach is a hybrid one, which uses a combination of Computational Fluid Dynamics (CFD) and Computational AeroAcoustics (CAA) based on an acoustic analogy (Harwood and Dupère, 2016).

In such a hybrid approach, the CFD analysis is a critical step because its results provide noise source information for the noise prediction of the next step. For industrial CFD simulations, one of the long-standing challenges is to generate an affordably sized grid with sufficient quality. Some numerical studies have been conducted for whole train models, including the bogies (Sima et al., 2008; Lan and Han, 2017; Zhu et al., 2017a; Dong et al., 2019; Liang et al., 2020). However, most of these studies focused on the general flow field without providing details of the grid used or the details of the flow field around the bogie. Due to its complex geometry, the discretisation of the region around the bogie with an appropriate CFD mesh becomes a bottleneck.

To discretise the domain using a structured hexahedral grid, Zhu et al. (2016) greatly simplified the bogie geometry, and only included the wheelsets and a highly simplified bogie frame. In the initial simulations, the bogie cavity under the train was omitted and for this situation the results indicated that the wheelsets produced a greater amount of dipole noise compared to that generated by the frame. Zhu et al. (2018) again utilized a structured grid approach to investigate the aerodynamic noise produced by a simplified bogie positioned within a bogie cavity, both with and without the inclusion of a fairing. It was found that the primary contributors to the dipole noise were pressure fluctuations resulting from vortex shedding and flow separation around the geometrical features. Due to the fairing the flow unsteadiness does not enter the bogie cavity and interact with bogie components, and this can reduce the pressure fluctuation outside the cavity, leading to a reduction of the far-field noise.

To discretise a bogie with complex geometry, He et al. (2021) introduced a hybrid grid technique, which combines hexahedral elements near solid surfaces and polyhedral elements in the remaining volume. This grid configuration was employed for simulating the dipole noise generated by a bogie with most of its components located in a simplified cavity. The results, which are consistent with the experimental research by Sawamura et al. (2021), showed that the rear part of the bogie had stronger noise sources than the front part, while the noise contribution from the cavity walls was dominant.

However, the numerical simulations considered above either have an insufficiently refined grid in the boundary layer regions, an oversimplified bogie structure, or do not consider the effect of the turbulent inflow from upstream.

To simulate wall-bounded flow accurately, especially in cases involving flow separation, the grid distribution in the boundary layer region is known to be particularly critical (Spalart and Allmaras, 1992; Shur et al., 1999; Spalart and Streett, 2001). In particular, the non-dimensional height of the first boundary layer grid y^+ should be sufficiently small, usually $y^+ < 1$ ($y^+ = yu_\tau/\nu$, where y is the distance of the first grid to the wall, u_τ is the friction velocity, and ν is the kinematic viscosity). This ensures sufficient resolution of the viscosity sublayer, which, although thin, is very important for accurate simulations of the shear stress and momentum transportation in the boundary layer (Craft et al., 2006). Therefore, to resolve the boundary layer flow, it requires a large proportion of the total number of grid cells to be assigned to this region. In the context of industrial simulations, wall functions, which are empirical algebraic formulae that can provide overall flow properties of the sublayers, could be used to reduce the number of grid cells within the boundary layer (Eça et al., 2015). The wall functions can usually provide flow properties such as velocity, shear stress, turbulent kinetic energy, and length scale. However, these flow properties are empirical or semi-empirical, making them suitable primarily for straightforward near-wall flows. With more complex, non-equilibrium flow, reliance on such properties can result in significant errors (Craft et al., 2004; Eça et al., 2015). Furthermore, to predict aerodynamic noise, which requires higher accuracy in predicting flow fluctuations (Carley, 2011), the quality and resolution of the boundary layer grid are even more critical. Thus, for simulations of aerodynamic noise generated by complex geometries, high resolution grids are preferred for the boundary layer.

It is pointed out by Guo et al. (2020) that simplification of the bogie geometry can significantly affect the high-speed train aerodynamics. In crosswinds, the increase in positive and negative pressures in the bogie cavities is affected by the degree of simplification of the bogie structure, whereas that on the cavity roof is mostly unaffected. Consequently, it is reasonable to suppose that, when the geometry of the bogies is unrealistic, the flow state will be also unrealistic and thereby the aerodynamic noise generated from the flow field will deviate from reality. Thus, to ensure the simulated flow that closely resembles practical one, the bogie geometry included in the model should be as realistic as possible.

To calculate the noise generated by a realistic leading bogie, the nose of the train should be included in the simulation model. Minelli et al. (2020) investigated the aerodynamic noise generated by the nose of an ICE3 train, without a bogie in the cavity, using compressible improved delayed detached eddy simulations (IDDES). The jet flow below the cowcatcher and the lateral shear layer at the sides of the cavity were investigated. It was found that the jet flow predominantly interacts with the ground surface and the components situated beneath the train, whereas the lateral shear layer flow impacts components in close proximity to the cavity's sides. Moreover, Guo et al. (2022) investigated the impact from cowcatcher clearance on leading car aerodynamics. It was also found that the state of the turbulence from upstream exerts a substantial influence on the surface pressure at the underside of the leading bogie, which is produced by the impingement from the turbulent flow through the cowcatcher clearance.

The aims of this paper are to investigate the aerodynamic noise generated by the leading bogie of a high-speed train and provide insight into its noise generation mechanisms. Numerical simulations of the flow field around the bogie are performed and the aerodynamic noise is predicted. The bogie model retains most of its components and, to consider the effect of the turbulent inflow from upstream, it is positioned beneath the leading car of a high-speed train. To guarantee a sufficient grid resolution within the boundary layer region, the hybrid grid system, which was explored by He et al. (2021), is further developed and applied to discretise the complex geometry. To facilitate feasible numerical calculations, the physical scale of the model and the inflow velocity have been reduced. The flow field around the leading bogie, the dipole noise source distribution on the solid surfaces, and the characteristics of the aerodynamic noise are calculated and discussed, revealing the dipole noise generation mechanisms.

The paper is organized as follows: Section 2 introduces the model geometry, numerical set-up, and the discretisation. Validation of the method is presented in Section 3. Section 4 provides an analysis of the aerodynamic results including the flow structures. The noise source analysis and the far-field noise are discussed in Sections 5 and 6. Finally, Section 7 presents the findings and conclusions of the study.

2. CFD case description and numerical settings

2.1. Model geometry and numerical settings

To carry out simulations for a more realistic case, a computational model is developed that contains a detailed bogie, retaining most of its components, installed beneath the leading car body, as shown in Fig. 1 (a). The car body encompasses a train nose, a cowcatcher situated

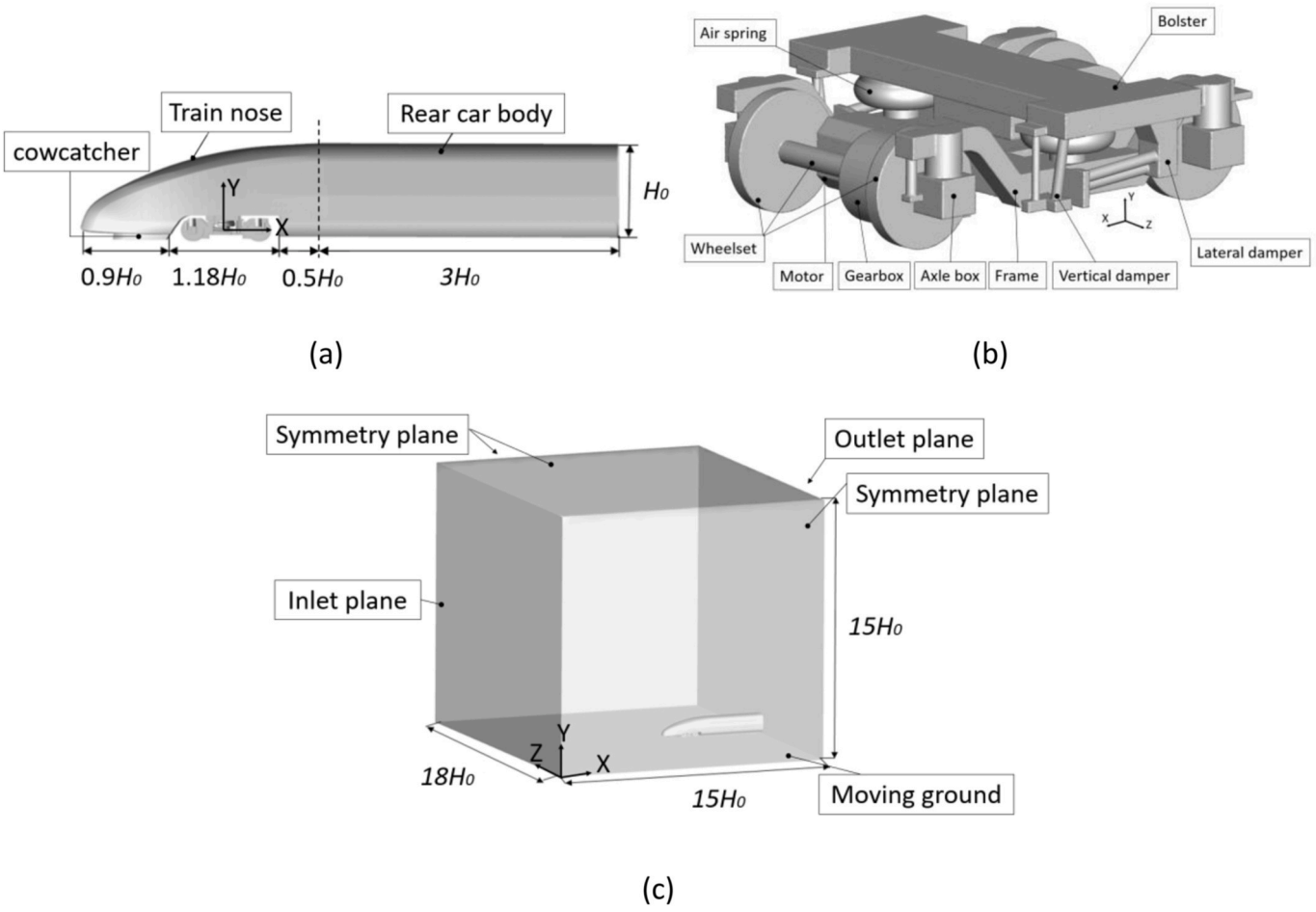

Fig. 1. Computational model and domain dimensions. (a) Side view of the model; (b) geometry of the bogie; (c) computational domain dimensions.

beneath it, a bogie cavity and part of the rear car body. The main dimensions are indicated in terms of the height of the train body H_0. The train nose section refers to the front part of the car body, up to a point that is $0.5H_0$ behind the rear wall of the bogie cavity. To attenuate potential influences from the outlet boundary condition at the downstream end, the first carriage is carefully truncated. This truncation is applied at a point $3.5H_0$ behind the rear wall of the bogie cavity, just before reaching the location of the second bogie cavity (which is omitted). The analysis focuses on the leading bogie; the slipstream, wake, and flow features related to subsequent bogie cavities and inter-car gaps are neglected.

Fig. 1(b) displays the bogie model, which is the same as used by He et al. (2021) and contains all the main bogie components. To compare the noise levels emitted by different parts of the bogie, it is categorised into three groups: the upstream and downstream 'dynamic' components and the frame. The upstream and downstream dynamic components include the respective wheelsets, gear boxes, motors, and axle boxes; the group of components associated with the frame includes the air springs, lateral and vertical dampers at the two sides, and the bogie frame itself.

To reduce the computational cost to a manageable level, both the physical size of the model and the incoming flow speed were scaled down. The model dimensions were reduced to 1/12 of the full scale; the flow speed was lowered to 10 m/s, equivalent to 1/11 of the original speed of 110 m/s or 400 km/h. The Reynolds number is 2.11×10^5 based on the height of train model H_0 (0.316 m) or 1.91×10^5 based on the width of the train model (0.287 m). The selection of this Reynolds number is based on the experimental research by Lauterbach et al. (2012). The Reynolds number of the computational model in Fig. 1 (a) exceeds the minimum Reynolds number of 1.53×10^5, based on the train width, established in the experiments of Lauterbach et al. (2012). This ensures that the results obtained are largely independent of Reynolds number. When choosing the scale ratios for the physical size and train speed, a size ratio close to the speed ratio was opted. This approach ensures that the Strouhal number is least affected, which enhances the similarity of the flow field between the scaled model and the original model in the frequency domain. The Strouhal number St is defined as follows:

$$St = \frac{fD}{U} \tag{1}$$

where f is the frequency of the oscillation, D is the characteristic dimension of the model and U is the flow speed relative to the model. The full speed of the train is taken as 400 km/h or about 110 m/s. An integer value for the scaled speed (10 m/s) was preferred when selecting the speed ratio. Thus, the scale ratio of speed is 1/11. However, for simplicity, the effect on the frequencies of the factor 11/12 has been neglected.

It is worth mentioning that this reduction of the Reynolds number may introduce a certain level of error to the absolute noise level when scaling it to the Reynolds number of High-speed trains. This is particularly true for the noise information at high frequencies, as it is typically generated by flow regimes that are less influenced by the dimensions of the bogie geometry but are more significantly affected by local viscous flow conditions. However, as indicated by the literature reviewed in the Introduction section, the bogie noise is dominated by low frequencies and the noise at high frequencies is of secondary importance. Furthermore, the results will pertain to the relative effects, such as the contributions to the sound pressure levels and sound power levels from

different components, as well as the areas identified with strong noise sources, are not expected to be significantly affected by the Reynolds number reduction.

The full computational domain is shown in Fig. 1(c), with dimensions defined in terms of H_0. To minimize the influence of the domain boundaries and improve the simulation stability, the front inlet plane is set at a distance of around $10H_0$ from the train nose. The distance between the two side planes is $18H_0$ and the top plane is around $14H_0$ away from the roof of the car body; this ensures the blockage ratio due to the train remains below 0.4%. In addition, for simplicity the ground is positioned 20.83 mm (scaled size) below the wheels while both the rails and the track structure are excluded, as also done by Minelli et al. (2020) and Guo et al. (2022). It should be noted that, for the sake of computational affordability, only the leading carriage will be simulated, while the rear part of the train will be omitted. As shown in Fig. 1(a), the truncation surface is located at $3.5H_0$ away from the rear wall of the cavity. A zero-pressure outflow boundary condition is set at the truncation surface. It should be noticed that the pressure on the truncation surface is not precisely zero, particularly in the boundary layer, due to the non-uniform outflow field. However, with carefully chosen distance (3.5 H_0) from the leading bogie region, the non-uniformity of the flow will decay and the flow field at the outlet plane will become considerably more uniform than upstream. Furthermore, at a certain distance downstream boundary, the pressure will tend to approach zero near the train's solid surface, even though it may not be exactly zero within the boundary layer (Zhang et al., 2018; Gao et al., 2019). The same boundary condition has been employed at the outlet plane in similar scenarios in numerical research conducted by Zhu et al. (2016) and Kim et al. (2020), and the numerical results demonstrate good agreement with the experimental data.

2.2. Numerical set-up

To facilitate the CFD simulations, a coordinate system centred on the train is adopted. In this coordinate system, the train remains stationary, while the ground and the incident flow move in the opposite direction at the running speed of the train. As seen in Fig. 1(c), the inlet plane is specified as a velocity inlet boundary condition (10 m/s) and the outlet plane is assigned a zero-pressure outlet boundary condition. Symmetry boundary conditions are applied to the two side and top planes. All solid surfaces of the computational model are set as non-slip walls. Zhu et al. (2017b) pointed out that the boundary condition applied at the ground has a significant impact on the flow under the bogie. Thus, to take account of the relative motion between the train and ground, the ground is specified as a moving wall with non-slip condition.

Considering that high-speed trains typically operate at speeds below a Mach number of 0.3, the incompressible Navier-Stokes equations are solved to obtain the unsteady flow field (Chung, 2002). To balance the simulation accuracy and computational cost, the Delayed Detached Eddy Simulation (DDES) is employed, using the Spalart–Allmaras (S-A) turbulence model (Spalart et al., 2006). The DDES method has been applied effectively in simulating aerodynamic noise for models with complex geometry, such as train bogies (Zhu et al., 2016; Guo et al., 2020) and airplane landing gears (Vuillot et al., 2012; Oza et al., 2016; Ricciardi et al., 2021). The noise calculations derived from the DDES method in OpenFOAM 2.4.0 have been validated through experiments conducted in previous research. This validation includes various basic geometric elements of the bogie, including circular cylinders (Liu et al., 2019), square cylinders (Liu et al., 2018), and cubes (Wang et al., 2019), and simplified bogie components such as isolated wheelsets (Zhu et al., 2017), tandem wheelsets (Zhu et al., 2016), and very simplified bogies (Zhu et al., 2016).

Prior to the unsteady simulation using DDES, the steady Reynolds-averaged N–S equations are solved, with the S-A turbulence model, to initialize the flow field. The flow simulation is conducted by using OpenFOAM 2.4.0. To maintain computational stability and simultaneously achieve sufficiently accurate results, in the discretisation of the divergence term, a second-order Total Variation Diminishing (TVD) scheme is implemented. For the convection term, the Gauss linear interpolation scheme is utilized. This scheme necessitates a grid that is of high quality and has a uniform distribution to deliver accurate results and maintain computational stability. A second-order implicit temporal scheme is chosen, which is known as "backward time marching" in OpenFOAM.

2.3. Grid strategy

As mentioned in Section 1, aeroacoustic simulations for flow over solid structures require high quality and fine resolution grids, especially within boundary layers. At the same time, the problem geometry is too complex to allow a structured grid to be used throughout. Therefore, a hybrid grid, as has been explored by He et al. (2021), was adopted to discretise the model shown in Fig. 1. A hexahedral grid is generated to cover the boundary layer around the solid surfaces and a tetrahedral grid is implemented in the region away from the walls. These grids are generated in ANSYS ICEM and the tetrahedral grid is finally converted to a polyhedral one in ANSYS Fluent.

The hexahedral grid for the bogie in the current simulations adopts the same grid density as suggested by the grid dependence study carried out for the same bogie by He (2023). In the boundary layer, there are 25 grid layers with an expansion ratio of 1.1 and the first grid near the bogie surface was adjusted to ensure the values of y^+ are smaller than 1; the maximum aspect ratios of the cells close to the bogie components range from 65 to 128, which is acceptable. To decide grid parameters for the car body, a half-width model without bogie was employed in a grid dependence study. The computational domain and boundary conditions remain consistent with those detailed in Section 2.2 apart from a symmetry condition that is applied at the mid-plane, which is due to halving the model. It should be noted that using a half-model and applying a symmetry boundary condition at the mid-plane will introduce some changes to the local flow. This is because the symmetry boundary condition prevents mass flow perturbations at the mid-plane. However, these perturbations are not expected to be significant because the car body is symmetrical at the mid-plane. Even though there may be some differences in the flow field near the cowcatcher area due to vortex shedding, it is not anticipated to affect the results of the grid study.

In the grid generation, three refinement zones have been implemented. The first zone encompasses the entire car body and employs the largest grid size. The second zone covers the train nose, cowcatcher, and the bogie region, using an intermediate grid size. The third zone, with the finest grid, is exclusively dedicated to the region covering the cowcatcher and bogie cavity, as these are the areas of primary interest in this simulation. Five cases were run with different mesh density, denoted by case A-E, as listed in Table 1. Case A has the coarsest grid; case B is a baseline case and has a finer grid than case A. The hexahedral grid remains unchanged in the wall normal direction, while refinements are exclusively applied in the streamwise and circumferential directions. Compared with case B, the surfaces of the train nose and cowcatcher are refined for case C, while in case D only the volume grid is refined. Case E has the finest grid in all regions. In all cases, the first layers of the hexahedral grid were carefully selected to maintain y + values below 1

Table 1
Key flow and grid parameters for grid refinement study.

Feature case	A	B	C	D	E
Max. aspect ratio	175	115	95	115	85
Refinement size (mm)	2.7	2.0	2.0	1.5	1.5
Number of cells (million)	3.9	8.4	10.1	9.9	15.5
C_d	0.151	0.139	0.140	0.139	0.136
C_l	−0.133	−0.129	−0.130	−0.130	−0.132
SPL (dB)	97.2	95.5	95.6	95.5	95.2

and the expansion ratio was consistently set at 1.1. The mesh around the train nose and within the bogie cavity was particularly refined.

Table 1 lists key flow and meshing parameters for the five cases. The mean drag coefficients for all cases, except case A, are found to be within 5% of the results obtained for case E, while the mean lift coefficients are within 2.3%. The sound pressure level (SPL) is also calculated at a receiver situated to the side of the train at 20 m from the bogie centre. The discrepancy in SPL is generally less than 0.5 dB except for case A, which exhibits a difference of 2 dB. Therefore, it is recommended to prioritize the grid parameters from case B when discretizing the full model. To improve grid quality at the junction with the bogie grid, localized variations in grid density are implemented when the bogie is included. These variations fall between those employed in cases C and D.

Based on this grid refinement study, and the one conducted by He (2023) for the bogie, the final grid of the full model shown in Fig. 1 is generated with about 36.4 million cells, which consist of 17.7 million hexahedral and 18.7 polyhedral cells. Fig. 2 illustrates the grid distribution in the bogie region, specifically in a horizontal plane through the wheel centres. As shown in the expanded view in Fig. 2(b), transitional hexahedral volume grids are strategically utilized to connect the boundary layer grid with the polyhedral volume grid wherever feasible. This improves the grid quality in the proximity of the interfaces, and it effectively mitigates any flow disruptions attributed to grid transitions at these interfaces. Furthermore, this is a good general practice as these interfaces are typically located near solid boundaries, where the flow undergoes rapid changes; it should therefore be applied whenever possible. In tight spaces, such as where the wheel surface closely approaches the axle box, as illustrated in Fig. 2 (b), great care is taken when creating a direct connection between these two different types of grid. The height of the outermost cell within the structured grid, positioned near the interface, is of great importance as it directly impacts the orthogonality of the nearby polyhedral grid. Therefore, it is imperative to endeavour towards maintaining a minimal discrepancy in volume between the adjacent hexahedral and polyhedral cells at the interface.

3. Methodology validation

The isolated wheelset case, previously studied through both experimental and numerical analyses by Zhu et al. (2014), is chosen to validate the numerical methodology employed in this study. As in the original study, the wheelset is modelled at a scale of 1:10 and, to reduce the computational cost, simulations were run for half of the wheelset with a symmetry condition applied at the centre plane, and the wheel shape was idealized to a flat disc. The diameter of the wheel is 92 mm and the inflow velocity is 30 m/s; other parameters of the wheelset geometry and computational domain can be found in Zhu et al. (2014).

The same hybrid approach is used as for the bogie simulations. The surface grid on the wheelset is shown in Fig. 3. In the boundary layer region, there are 25 prism layers based on a stretching ratio of 1.1. The

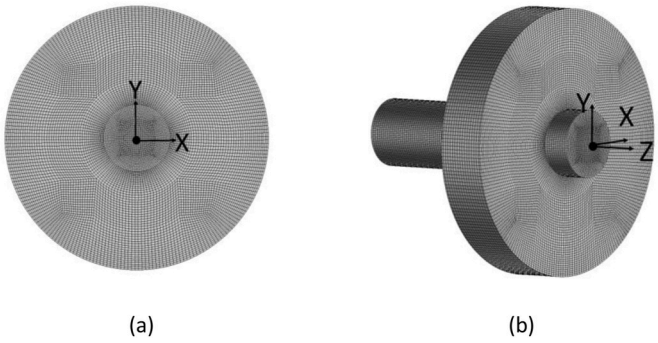

Fig. 3. Wheel surface grid. (a) Front view; (b) oblique view.

first boundary layer grid is fine-tuned to ensure that y^+ on the wheel surface remains below 1. In addition, there are 10 additional transition layers located outside the boundary layer to facilitate a smooth transition from the structured grid to the polyhedral one. In the polyhedral volume grid, two refinement zones are established around the wheelset. The inner one encloses the wheelset, while the outer one surrounds it and is three times larger. In the inner zone, the maximum mesh size is 1 mm, while in the outer zone it is 5 mm. The structured mesh employed by Zhu et al. (2014) had 5.5 million cells, whereas, in the current simulation, it has been reduced to approximately 3.2 million by employing the hybrid grid.

The numerical approach introduced in Section 2.2 is consistently applied in the current simulation. In the unsteady DDES simulation, a physical time step of 3×10^{-6} s is used to maintain a maximum Courant–Friedrichs–Lewy (*CFL)* number below 3.5. Data collection for flow statistics and noise source information commences after 0.4 s. The total data sampling time is 0.55 s, which is roughly equivalent to passing the wheel diameter 180 times.

Fig. 4 shows the noise spectra at two receiver locations used by Zhu et al. (2014). These are defined based on the coordinate system shown in Fig. 3, with the origin located at the outer end of the axle. The top receiver is located at (−0.018, 1.375, 0.0313) and the side receiver at (0, 0.185, 2.2113), in which the dimensions are all given in metres. To compare with data from Zhu et al. (2014), the power spectral densities (PSD) were converted to SPL spectra with $\Delta f = 6$ Hz. The current results from the hybrid grid agree with those from the structured hexahedral grid of Zhu et al. (2014). In comparison to the measurements conducted by Zhu et al. (2014), the spectra are predicted with a similar shape, with variations in the peak frequencies being under 3%. In Fig. 4(a), at the top receiver, the numerical predictions of the peak using both methods exceed the measured one by approximately 5.5 dB. This difference may be due to approximations introduced in the CFD model, such as modelling the wall as a symmetry plane, as explained by Zhu et al. (2014). In Fig. 4(b), at the side receiver, the background noise in the

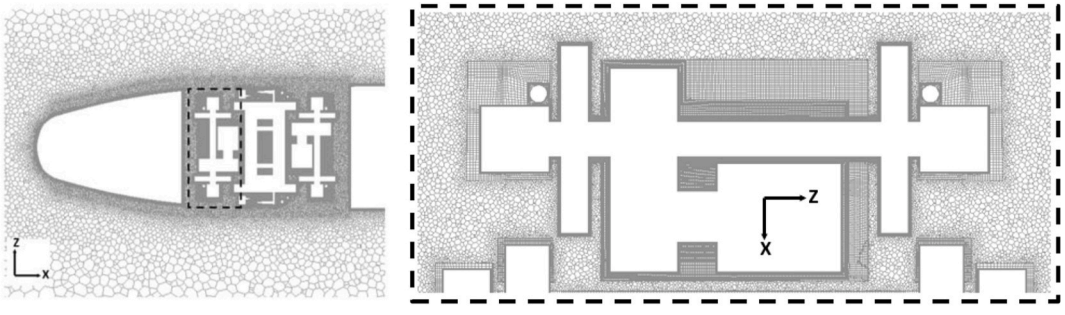

Fig. 2. Mesh distribution on a horizontal plane in the domain. (a) Overall view of the mesh on a horizontal slice; (b) local enlarged view (rotated 90° clockwise).

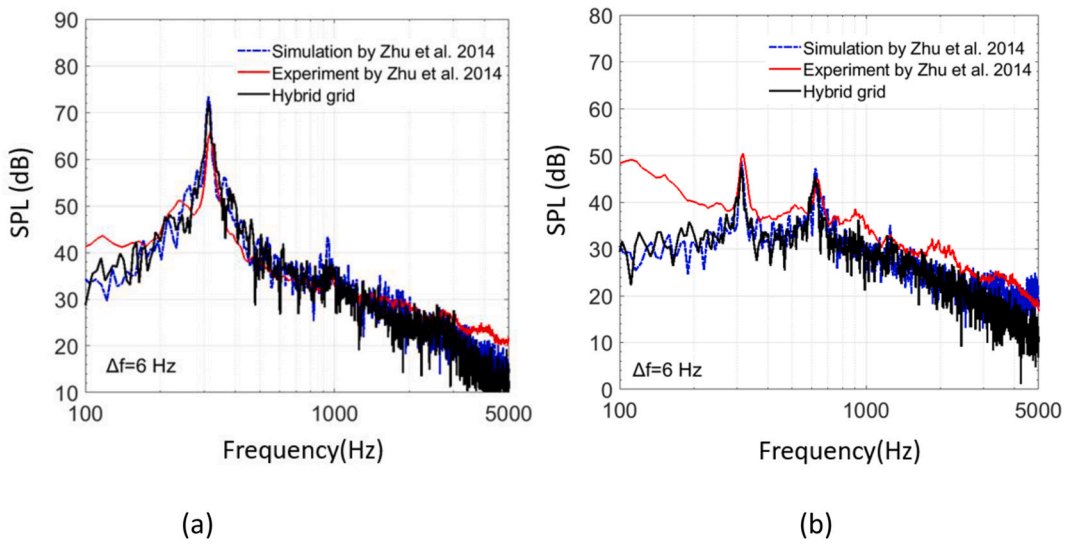

Fig. 4. Comparisons of the far-field noise spectra. (a) Top receiver; (b) side receiver.

wind tunnel has a significant impact on the experimental results, particularly at low frequencies, as noted by Zhu et al. (2014). Consequently, these values are higher than those obtained from the numerical results. However, the peaks in the numerical and experimental results are very close, with a difference smaller than 1.5 dB.

Based on these simulation results, it can be inferred that the performance of the hybrid grid is comparable to that of the structured hexahedral grid. The agreement between the numerical results and experimental data further validates the both the hybrid grid concept and the numerical settings adopted in Section 2.

4. Aerodynamic results

Before the unsteady simulation for the complete model depicted in Fig. 1 was conducted, a steady RANS simulation was performed using the S-A turbulence model to initialize the flow field. The steady calculation required approximately 4000 iterations to achieve convergence. The unsteady simulation was conducted using a physical time step of 2×10^{-5} s, ensuring that the maximum *CFL* remains below 5. The simulation is conducted for approximately 4.3 s, which corresponds to 120 flow-through times of the bogie cavity. Data collection begins once the simulation reaches statistical stability, a process requiring approximately 0.6 s, and it concludes when the statistical convergence is achieved in the collected force coefficients. The computational wall-time for this process totalled about 650 h, utilizing 640 processors on the Iridis5 cluster at the University of Southampton.

Fig. 5 displays the mean flow streamlines around the leading car. As indicated by the red arrows in Fig. 5(a), at the bottom, the flow from upstream is split by the cowcatcher. At the cowcatcher front edge, a portion of the flow separates and travels beneath it toward the bogie cavity, exerting a substantial influence on the flow dynamics within the cavity. Meanwhile, the rest of the flow moves along both sides of the cowcatcher (Fig. 5(b)). As can be noted in Fig. 5(c), the flow along the side of the cavity comprises two distinct components. One component originates from the streamlines split by the train nose, with a portion entering the cavity and contributing to the formation of vortices at the rear section of the bogie cavity, as highlighted by the blue arrows in Fig. 5(c). The other component results from the flow division by the cowcatcher front face, leading to the creation of vortices at the front of the cavity, as denoted by the red arrows in Fig. 5(c). Those vortices cause strong unsteadiness in the cavity flow, which interacts with the bogie and generates aerodynamic noise sources.

The presence of the bogie cavity provides some shielding to the bogie, resulting in a less impact on the inner components from the upstream flow compared to the outer components. To provide a detailed

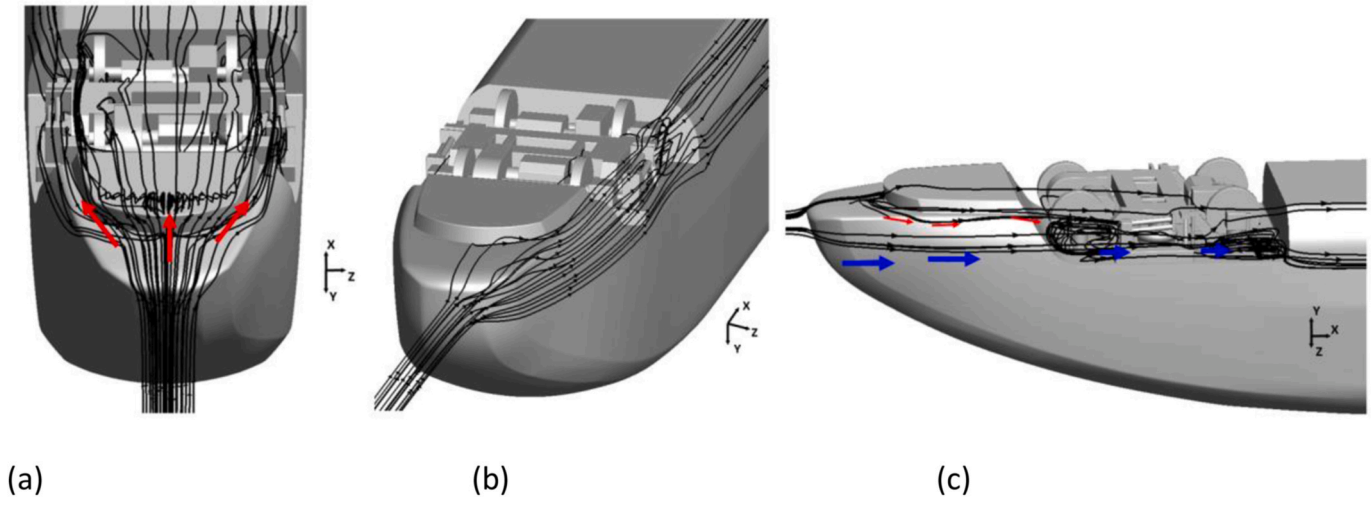

Fig. 5. Mean streamlines for flow over the leading car nose. (a) Bottom streamlines; (b) side streamlines; (c) vortex streamlines in the cavity.

view of the flow field around the bogie, Fig. 6 displays the streamlines on three slices superposed with contours representing the mean streamwise velocity. Fig. 7 shows the instantaneous pressure coefficient:

$$C_p = p \Big/ \left(\frac{1}{2}\rho U_0^2\right) \tag{2}$$

where p is instantaneous pressure, ρ is the density of air and U_0 is free-stream velocity) on two of these three planes. Figs. 6(a) and Fig. 7(a) show a horizontal slice at the centre of the axles. As a result of the curvature of the train nose, the flow velocity at the leading edge of the cavity increases to approximately $1.1U_0$ after being split by the train nose. Subsequently, the shear layer along the side surface of the train separates from the leading edge of the cavity. Low pressure cores within the shear layer can be clearly seen in Fig. 7(a), which are characterized as shear vortices (Minelli et al., 2020). These vortices are generated due to the Kelvin-Helmholtz instability within the shear layer, a phenomenon that typically arises in separated shear layers around bluff bodies (Brun et al., 2008). As the flow develops further downstream, the detached shear layer disperses. Some large vortices, formed within the shear layer, penetrate into the cavity propelled by the high-speed flow from the train side. These vortices have a notable effect on the rear section of the cavity and the bogie, particularly on components situated near the outside of the cavity.

Fig. 6(b and c) show the detailed flow field on two vertical slices that pass through the centres of the bogie and the middle of the wheels. Notably, the incoming flow experiences acceleration to approximately $1.25U_0$ beneath the cowcatcher due to the decreased gap under it. Additionally, it can be noted from Fig. 7(b) that a separation zone appears immediately following the front edge of the cowcatcher. This separation zone causes increased blockage, consequently leading to a further acceleration in the flow under the cowcatcher. Subsequently, as the flow exits the cowcatcher region and enters the cavity, it experiences a sudden expansion, resulting in a significant reduction in velocity, particularly towards the rear section of the cavity. Unlike the two sides of the cavity, a greater flow is entrained into the cavity from underneath, as shown in Fig. 6(b) and (c). Within the cavity, the airflow circulates at a considerably lower speed, flowing from the rear to the front along the roof of the cavity. Therefore, it seems that the outer parts of the bogie, including the bottom and its two sides, are more affected by the turbulent flow from upstream.

The discussion above showed that the bogie is exposed to the turbulent shear layer separated from the front edges of both the cowcatcher and the cavity. It is expected that this interaction between the exposed components and the shear layer would produce strong noise sources. In Fig. 8, the turbulence structures are visualized through the presentation of iso-surfaces of Q_{norm}, which is the normalized Q criterion. The Q criterion represents the second invariant of the gradient of velocity:

$$Q = 1/2\left(\Omega_{ij}\Omega_{ij} - S_{ij}S_{ij}\right) \tag{3}$$

where $\Omega_{ij} = 1/2(\partial u_i/\partial x_j - \partial u_j/\partial x_i)$ is the vorticity tensor and $S_{ij} = 1/2(\partial u_i/\partial x_j + \partial u_j/\partial x_i)$ is the strain rate tensor. Q_{norm} is calculated:

$$Q_{norm} = Q \Big/ (U_0/H_0)^2 \tag{4}$$

where U_0 represents the free stream speed and H_0 is the car body height. The plot corresponds to a value of 12. The iso-surfaces are coloured based on the normalized time-averaged streamwise velocity $\overline{U}/U_0$.

Fig. 8(a) shows the bottom view of the model, from which the vortices emanating from the front section of the cowcatcher are clearly visible. As illustrated in Fig. 5(a), the incoming flow encounters the cowcatcher and subsequently separates at its front edges, creating a wake with high turbulence intensity beneath the train. The flow also moves along the cowcatcher's sides and separates towards the termination of its arc. This separation leads to the creation of a detached wake at the cavity front edge, clearly observable in Fig. 8(b), which gives a side view of the model. Consequently, the components of the bogie are situated within the intense turbulent wake and are exposed to a complex incoming flow. In addition, the vortices behind the bogie cavity disperse much more rapidly compared with the flow patterns established at the bogie region. Considered together with the mean velocity shown in Fig. 6, it appears that the rear wall of the cavity impedes further development of the wake. Some of the vortices in the wake enter the cavity, impinge on the cavity rear wall and deform, as was also found by Zhu et al. (2016). This turbulent flow entrainment causes large pressure fluctuations on the cavity and bogie surfaces, especially on the cavity rear wall and surfaces of bogie side components.

Fig. 9(a and b) show the instantaneous spanwise vorticity field on two slices at different spanwise locations, along train mid-plane and through wheel centre-plane. The wake that separates from the cowcatcher exhibits significant vorticity. As it progresses downstream, impingement by the strong vortical wake occurs on the lower segments

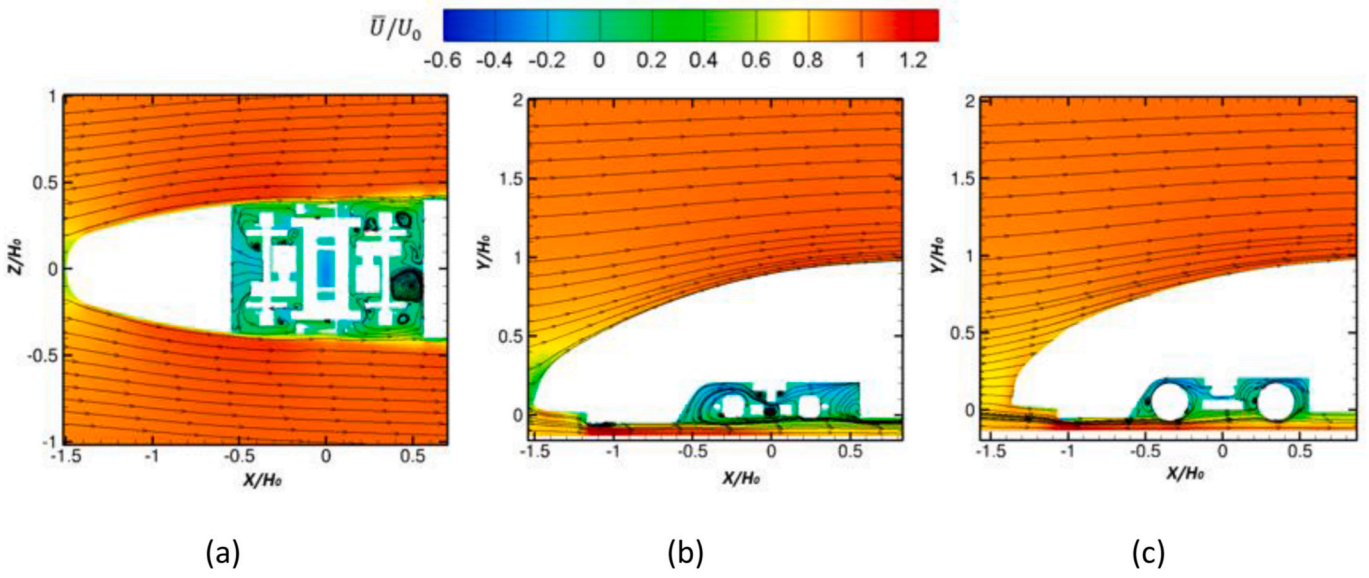

Fig. 6. Contours of the mean streamwise velocity and 2D streamlines on slices. H_0 is the height of the car body. (a) Horizontal slice through the wheel centres; (b) middle vertical slice; (c) vertical slice through wheel centres.

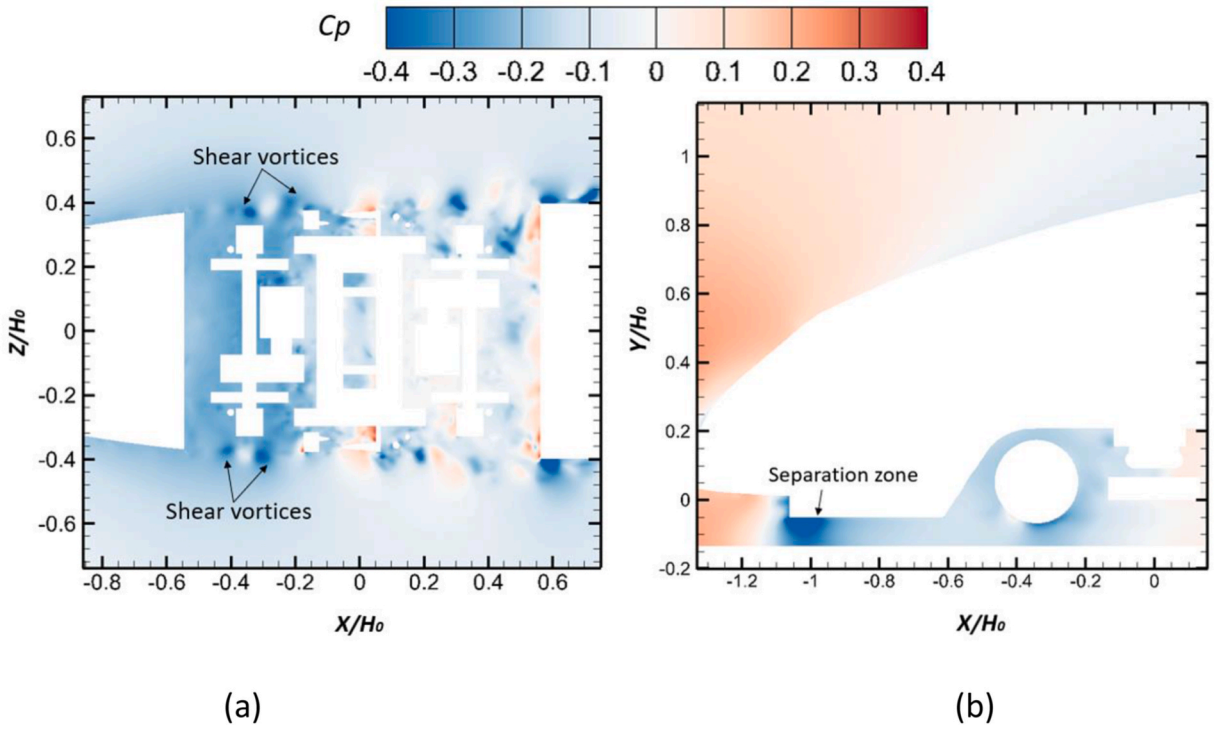

Fig. 7. Instantaneous field of pressure coefficient C_p on 2D planes. H_0 is the height of the car body. (a) Horizontal slice through the wheel centres; (b) vertical slice through the wheel centre.

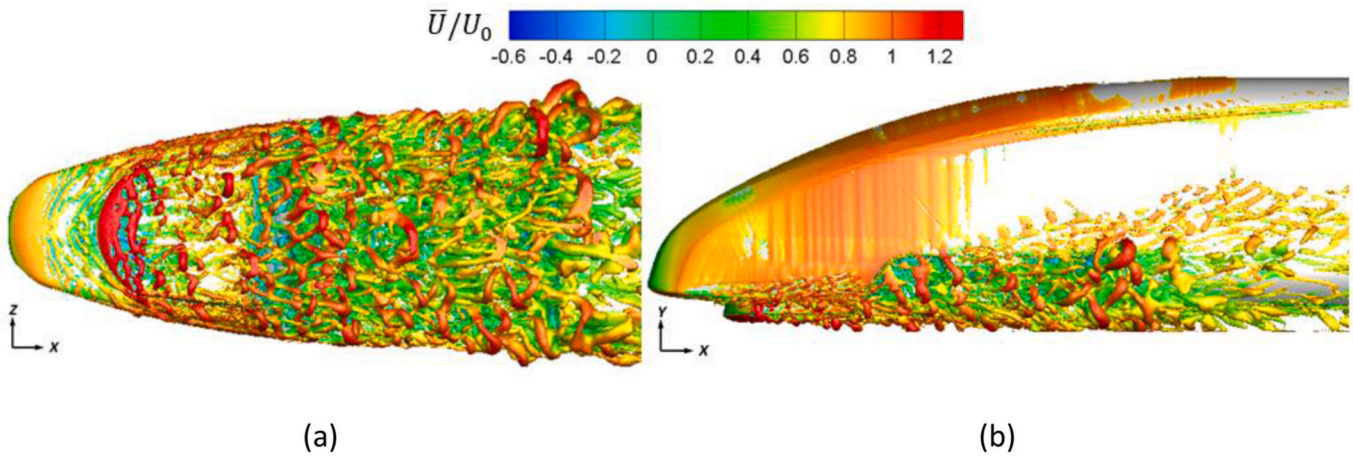

Fig. 8. Instantaneous flow structures represented by $Q/(U_0/H_0)^2$ at a value of 12, coloured by $\overline{U}/U_0$. (a) Bottom view of the model; (b) side view of the model.

of the bogie front components, including the underside of the frame, the front motors, and wheels. This impingement elevates the wake turbulence intensity, resulting in a more extensive dispersion of the wake. Consequently, a larger portion of the bogie's rear components are subject to the turbulent flow within the wake, which introduces high intensity pressure oscillations on their surfaces and will generate significant dipole noise. This is shown clearly in the horizontal slice through the centre of the axle, given in Fig. 9(c). The detached shear layer interacts with the bogie side components, including the axle boxes and the side dampers. This is the main reason, as will be analysed in more detail in next section, why the rear part of the cavity has stronger noise sources than the front.

5. Noise source analysis

As discussed in Section 4, the flow field in the bogie region exhibits high complexity and unsteadiness; this generates strong pressure oscillations on the surfaces of the bogie and cavity, which form the sources of dipole noise. The dipole noise sources originate from the presence of solid surfaces. This presence either generates or amplifies unsteady flow phenomena, such as vortex shedding, flow separation (Wang et al., 2005) or impingement. In the context of far-field noise analysis, the rate of pressure change, denoted as dp/dt, on the surface can serve as an indicator of sound source strength (Curle, 1955). To locate areas with strong noise sources, Fig. 10 displays its level, integrated across the frequency ranging from 20 Hz to 1600 Hz:

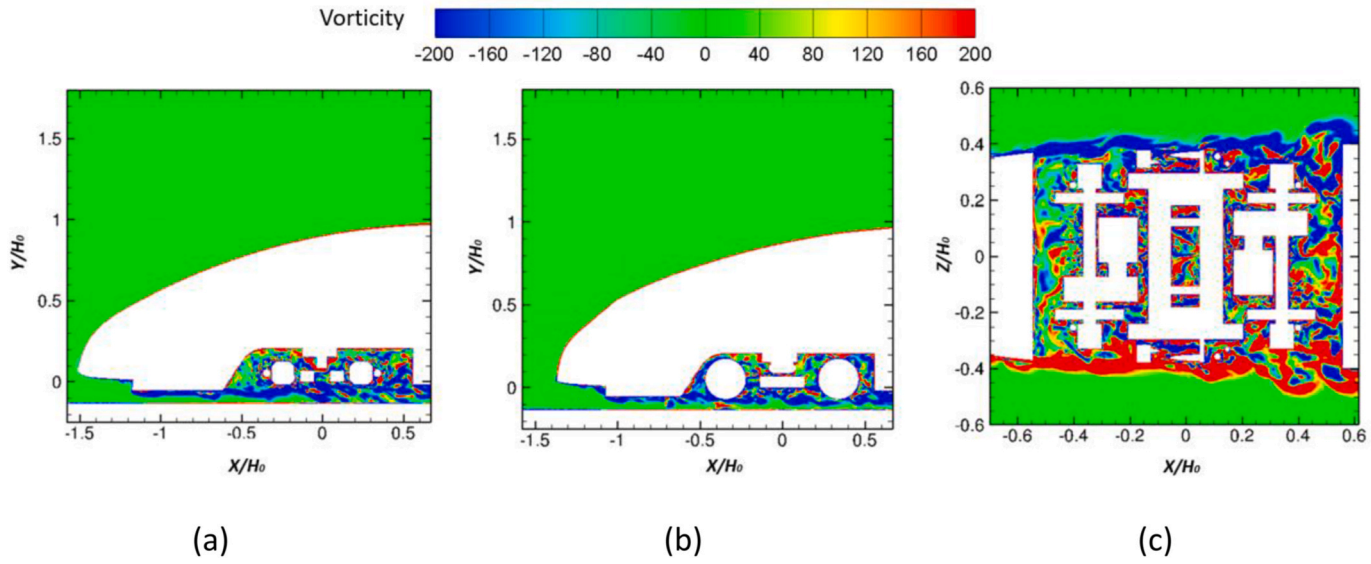

Fig. 9. Contours of instantaneous vorticity. H_0 is the car body height. (a) Vorticity in middle vertical slice; (b) vorticity in vertical slice through wheel centres; (c) vorticity in horizontal slice through the wheel centres.

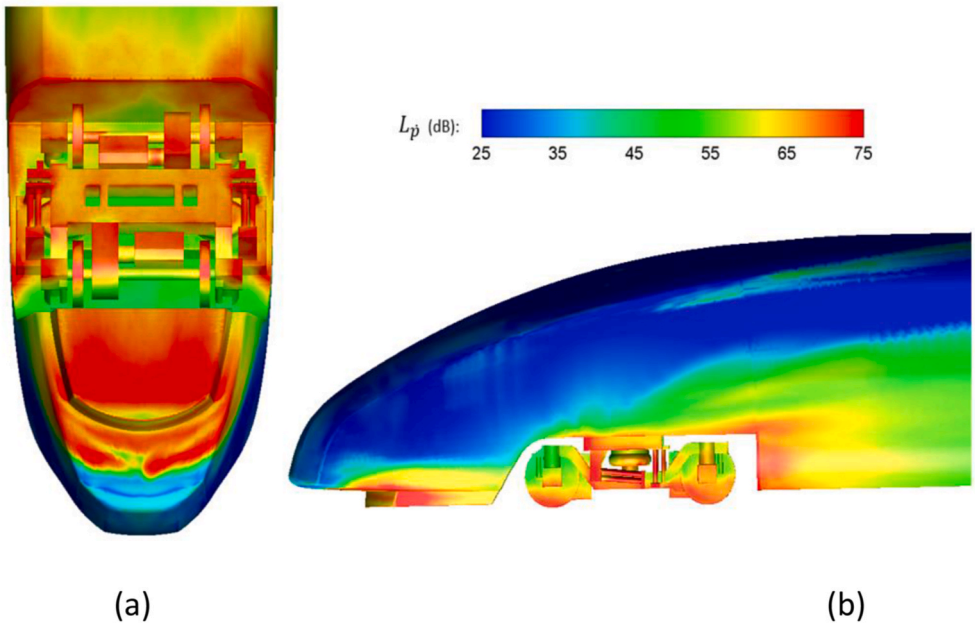

Fig. 10. Contours of the rate of pressure change, dp/dt, on the bogie components surfaces, integrated across 20–1600 Hz. (a) Model bottom view; (b) model side view.

$$L_{\dot{p}} = 10\log_{10}\left(\int_{f_1}^{f_2} PSDdf\right) \tag{5}$$

where PSD is the power spectra density of the dp/dt signal; f_1 and f_2 are the integral frequency limits.

Fig. 10 reveals that the lower portion of the model, encompassing both the cowcatcher and the lower surfaces of the components of the bogie, exhibits significant noise sources. This phenomenon is attributed to the interaction of this region with the strong turbulent wake, as depicted in Fig. 8(a), which separates from the cowcatcher front edge. This observation aligns with the experimental findings reported by Nagakura (2006). Although the cowcatcher is positioned at a lower level compared to all the bogie components except for the wheels, it appears that the bogie components do not receive significant shielding benefits. This is because of the abrupt flow expansion occurring behind the cowcatcher as it enters the bogie cavity. This expansion causes the high-speed flow beneath the cowcatcher to spread when entering the bogie area, subsequently introducing the turbulent wake into the cavity.

Strong pressure fluctuations are also evident on the bogie side components, including the vertical dampers, lateral dampers, and the side sections of the bolster. This region is primarily influenced by the shear layer separated from the cavity side edges, as illustrated in Fig. 9 (c). The lateral dampers, exposed directly to the detached shear layer, exhibit substantial pressure fluctuations on all surfaces. Additionally, the cavity rear wall is also subject to significant pressure fluctuations. As previously discussed, the presence of the cavity rear wall exerts a significant impact on the distribution of noise sources on both the bogie and the cavity. On one hand, it obstructs the downstream progression of

the turbulent wake, leading to pronounced pressure fluctuations on the wall due to wake impingement. On the other hand, the impeded wake flow generates vortices in the rear section of the cavity, as depicted in Fig. 6(a). As a result, a larger area of the rear section of the bogie is covered by intense pressure fluctuations. This finding aligns with the conclusions drawn from the experimental study conducted by Sawamura et al. (2021).

The contours of $L_{\dot{p}}$ at three different frequencies are displayed in Fig. 11. The integration bandwidth ($f_2 - f_1$) is 2 Hz, with centre frequencies of 30 Hz, 100 Hz and 1000 Hz. It can be observed that the intense pressure fluctuations at 100 Hz and below cover the largest area within the bogie region, while those at 1000 Hz cover the smallest area. This observation suggests that the noise source from low frequencies is expected to make a primary contribution to the far field noise, while the contribution from high frequencies is anticipated to be secondary.

The above discussion highlights the critical role played by the detached shear layer originating from the cavity front sides and the wake flow formed beneath the cowcatcher. These factors significantly influence the local flow dynamics around the bogie region and are expected to contribute to the generation of noise sources in these specific areas. This conclusion is consistent with that of the experimental research from Nagakura (2006).

6. Far-field noise

The far-field acoustic pressure is computed utilizing the Formulation 1A of Farassat (2007), which is the time-domain solution of the Ffowcs Williams and Hawkings equations, with the time-varying pressure on the solid surfaces as input. 36 receivers are set in a circle of radius 20 m around the bogie at an interval of 10°. Free space Green's functions are used and therefore effects of shielding and scattering by the car body and bogie structure and reflections from the ground are not considered.

The PSD of the sound pressure signals is determined using Welch's method, employing a Hanning window with a 50% overlap for each segment. Each segment has a duration of approximately 0.4 s, yielding a frequency resolution of 2.5 Hz. Then, these spectra are integrated into one-third octave bands after being rescaled to correspond to the full-scale train at 400 km/h. According to the dimensional analysis in Curle's theory (Curle, 1955), the sound intensity I generated by a dipole noise source conforms to the following relations:

$$I \propto \rho_0 c_0^{-3} U^6 D^2 r^{-2} \tag{6}$$

where ρ_0 is the air density, c_0 is sound speed in air, U is the flow speed, D is the typical size of the source and r is the receiver distance to the source. Therefore, the sound pressure level of the model can be scaled using the following equation:

$$\Delta SPL = 10\log_{10}\left[\left(\frac{D_1}{D_2}\right)^2\left(\frac{U_1}{U_2}\right)^6 \Big/ \left(\frac{r_1}{r_2}\right)^2\right] \tag{7}$$

where ΔSPL is the adjustment to the sound pressure level, D_1/D_2 is the geometry ratio, U_1/U_2 is ratio of the speed and r_1/r_2 is ratio of the receiver distance. Subscript 1 represents the full-scale situation, and 2 corresponds to the scaled model. For the frequency scaling, the Strouhal number St in formular (1) remains unchanged and the frequency can be scaled using the following equation:

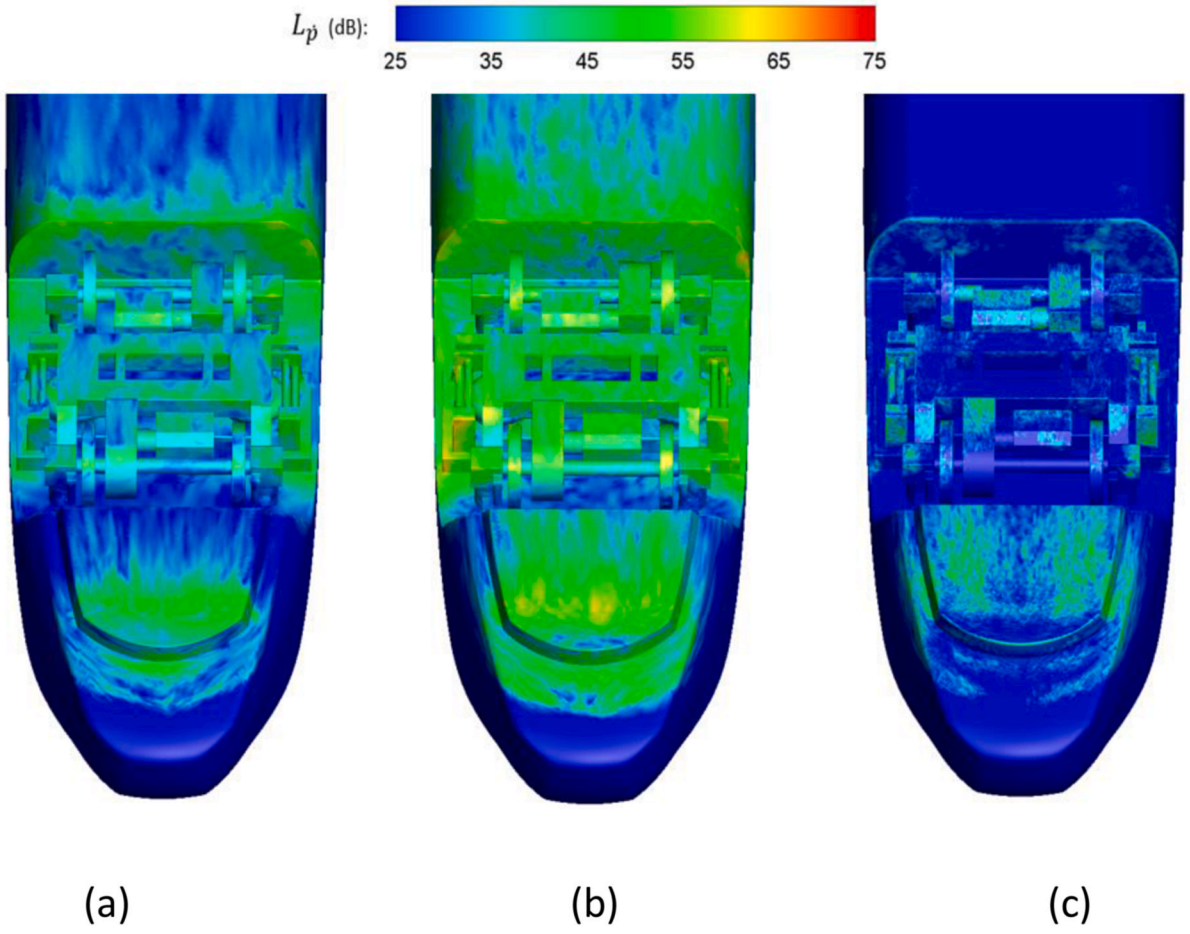

Fig. 11. Contours of the rate of pressure change, dp/dt, on the bogie components surfaces, integrated around different frequencies with 2 Hz bandwidth. (a) 30 Hz, (b) 100 Hz, (c) 1000 Hz.

$$\frac{f_1}{f_2} = \left(\frac{U_1}{U_2}\right) \times \left(\frac{D_1}{D_2}\right) \tag{8}$$

in which f_1/f_2 is the frequency ratio. Fig. 12 presents the one-third octave band noise spectra for the car body, the bogie and their combined spectrum at a horizontal receiver positioned at the same height as the bogie centre. In Fig. 12, the highest frequency is 2000 Hz and the SPLs at higher frequencies are not displayed because they are of secondary importance for the bogie noise. These spectra display broadband characteristics without discrete peaks. Notably, the noise spectrum of the bogie is consistently lower than that of the car body across all frequencies. Additionally, the noise levels around 50–160 Hz are higher than those in other frequency regions, which aligns with the noise source analysis in Fig. 11 and the results of the experiment conducted by Lauterbach et al. (2010).

Fig. 13 presents the overall SPLs produced by the bogie, the car body, and their total values, recorded across the circular arrangement of receivers. In general, the noise exhibits an almost omnidirectional distribution. The car body generates higher noise levels than the bogie does, with an approximately 8 dB difference in the upper direction. This can be attributed to the extensive shielding of the bogie from incoming airflow by the cavity, resulting in a considerably lower flow velocity inside the cavity compared to the external flow, as shown in Fig. 6.

The overall SPL contributions from different bogie components are shown in Fig. 14. At the lateral receiver (0°), the most substantial contributions come from the wheelsets (upstream and downstream). Among the frame components, the lateral side dampers make the most significant contribution, with a noise level similar to the gearboxes. At the vertical receiver (90°), notable noise contributions arise from both the frame surface and the axle boxes. These components exhibit pronounced noise sources on their lower surfaces, see Fig. 10.

The calculated sound pressure levels have been determined using the free space Green's functions. In reality, the car body would act as a shield for the sound waves in the upward direction. Furthermore, the car body and the ground would reflect the sound wave. However, it is expected that this model limitation is unlikely to have a significant impact on the total sound power generated by the various sources.

To gain deeper insights into noise contributions from various components and to identify critical areas for noise mitigation, the sound power level (SWL) emitted by the various components is examined. A sphere with a radius of 20 m, which encloses the entire model, was almost uniformly divided into 486 patches, with their central points designated as receivers. The SWL is obtained by integrating over the sphere:

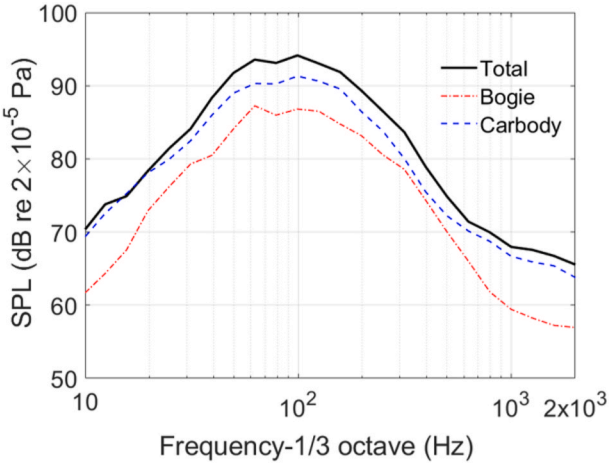

Fig. 12. Noise spectra of the model (1/3 octave), rescaled to full size, at the horizontal receiver at 20 m distance.

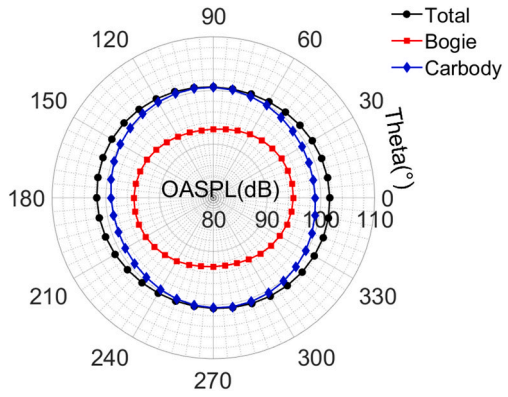

Fig. 13. The far-field noise in a vertical plane at 20 m distance.

$$SWL = 10\log_{10}\left[\left(\oint_S \frac{p_{rms}^2}{\rho c_0} ds\right) \Big/ W_{ref}\right] \tag{9}$$

where p_{rms} is the rms acoustic pressure, ρ is the air density, c_0 is sound speed in air, S is the sphere surface, ds is the segment area, and $W_{ref} = 10^{-12}$ W is the reference sound power value.

The proportion of the sound power produced from each component is shown in Fig. 15. As identified in Fig. 1(a), the car body is divided into different regions. The cavity walls produce the highest sound power contribution, as seen in Fig. 15(a). Based on the noise source distribution depicted in Fig. 10, it is evident that the rear section of the cavity is the primary area with the highest contribution to noise. Furthermore, the assessment includes the sound power generated by the ground (it was neglected in the sound pressure results earlier). This is the second highest component and occurs due to the high-speed flow beneath the cowcatcher, seen in Fig. 6(b and c). The sound power emitted by the entire bogie exhibits a similar level to that generated by the train nose and is approximately 5 dB lower than the combined sound power of the train body components. Although the cowcatcher and car body exhibit strong noise source regions, as evident in the dp/dt results presented in Fig. 10, they contribute less to the overall sound power due to the limited total area covered by the strong noise source. As seen in Fig. 9, the outer bogie components, such as the wheelsets and the lateral damper, are either fully exposed to the turbulent wake originating upstream or possess a substantial surface area that interacts with this turbulent flow, such as the lower surface of the frame. Therefore, as illustrated in Fig. 15(b), these four components contribute significantly to the sound power from the bogie. In the dynamic systems, the upstream and downstream gearboxes and axle boxes make a moderate contribution to the overall noise levels. Although they benefit from some shielding provided by the cavity, the turbulent wake impinges upon their lower surfaces, generating strong noise sources, as shown in Fig. 10. Other components, including the vertical dampers, the motors, and air bags, make minor contributions as they are mostly shielded by the cavity or upstream components or have relatively small surface areas.

From the above analysis, it is reasonable to conclude that, to reduce the radiated sound power, the most important regions are the rear sections, with a specific emphasis on the rear wall of the cavity, as well as the ground below the cowcatcher and the bogie. The ground generates a significant sound pressure in the vertical direction but considerably less in the horizontal direction. Therefore, in free space, it may not be significant for receivers located at the sides of the bogie. However, it can become important in practice, as the radiated sound may be redirected towards the sides. Regarding the sound power generated by the bogie, the most critical components are those that come into direct contact with the shear layer and the highly turbulent wake originating from the upstream components.

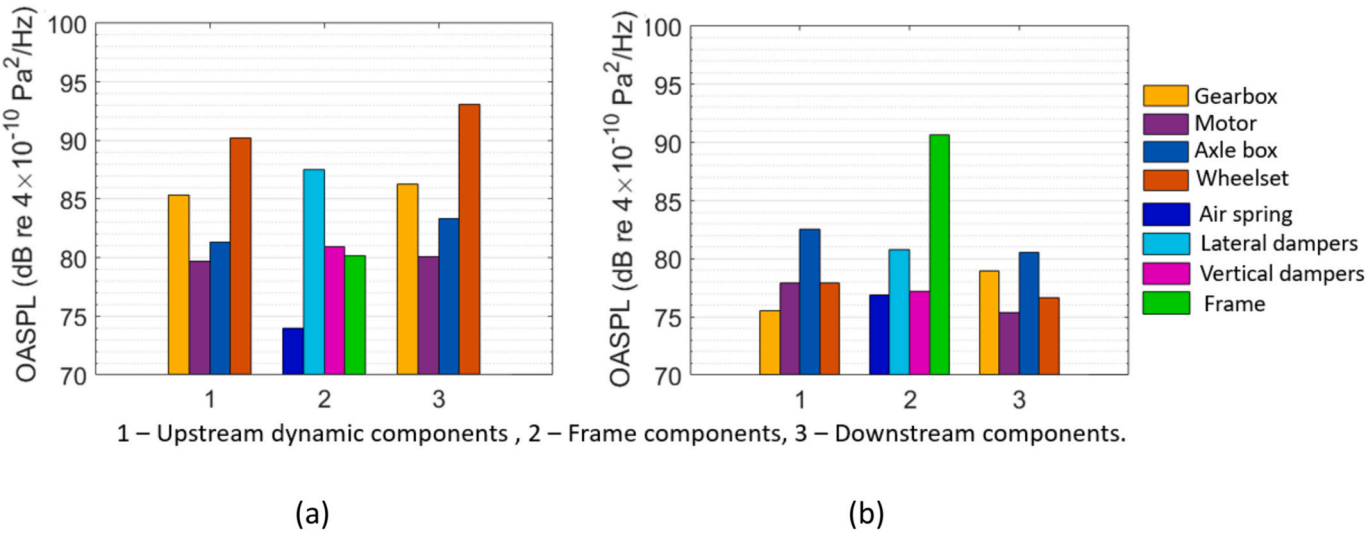

Fig. 14. Noise levels from bogie components at lateral and vertical receivers at 20 m distance. (a) 0°; (b) 90°.

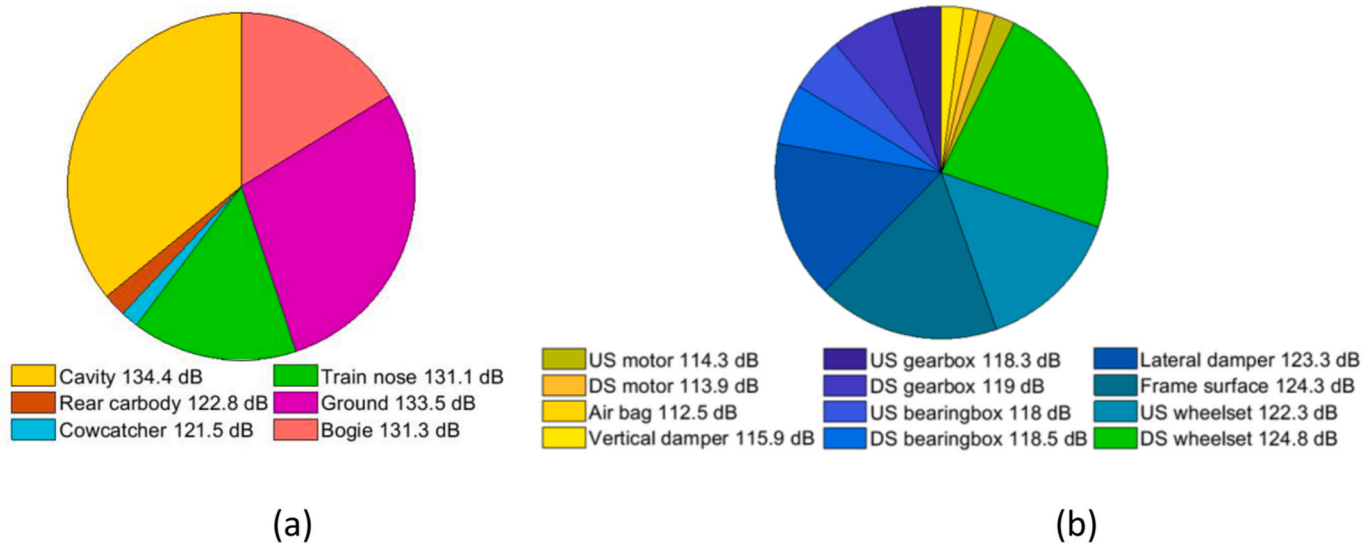

Fig. 15. Sound power contribution of different components. (a) Whole bogie and car body components; (b) components of bogie.

7. Conclusions

Numerical simulations have been conducted to study the aerodynamic noise produced by a high-speed train bogie beneath the leading car. The noise generation mechanisms have been analysed based on the results of the simulations of the flow field around the bogie and aerodynamic noise generated by its components. In simulations of the flow field, a hybrid grid system is introduced to facilitate the mesh generation around the complex bogie geometry, maintaining a sufficient resolution with practical grid size. The unsteady flow has been solved using the DDES method and the radiated sound is determined using the Ffowcs Williams and Hawkings equations. Strong noise sources are identified in areas that directly interact with turbulent wake and detached shear layers. These areas comprise the rear wall of the cavity, the side dampers, and the bottom of the cowcatcher and bogie. These observations are consistent with findings from Sawamura et al. (2021).

The sound power produced by the bogie is approximately 5 dB lower than that generated by the car body. This is primarily because the cavity shields the majority of the bogie from the turbulent flow. The largest contributors to sound power are the cavity walls and the ground beneath the train. Among the bogie components, the lateral dampers, the frame surface, and the wheelsets make the most significant contributions to the sound power. Furthermore, different bogie components contribute differently to sound pressure levels in the horizontal and vertical directions. In the horizontal direction, the wheelsets have the highest impact on the bogie noise, while in the vertical direction, the frame surface plays a more significant role.

In conclusion, for effective noise reduction, it is essential to address two crucial flow patterns: the shear layer detached at the two sides of the cavity and the wake flow with high turbulence intensity separated from the cowcatcher front edge. Furthermore, it is crucial to reduce the strong noise sources on the rear part of the cavity and on the ground to mitigate noise effectively. These findings confirm the cause of the noise source at the lower part of the leading car inferred in the experimental study by Nagakura (2006) and Sawamura et al. (2021), and enhance the understanding of the characteristics and generation mechanisms of the bogie aerodynamic noise, which can facilitate the development of noise reduction measures.

CRediT authorship contribution statement

Yuan He: Conceptualization, Data curation, Formal analysis, and

interpretation of data, Methodology, Writing – original draft. **David Thompson:** Conceptualization, Supervision, Writing – review & editing. **Zhiwei Hu:** Supervision, Writing – review & editing.

Declaration of competing interest

The authors declare that they have no known competing financial interests or personal relationships that could have appeared to influence the work reported in this paper.

Data availability

Data will be made available on request.

Acknowledgements

The research described in this work received support from the Ministry of Science and Technology of China through the National Key R&D Programme grant 2016YFE0205200, 'Joint research into key technologies for controlling noise and vibration of high-speed railways under extremely complicated conditions'. All simulations were conducted on Iridis5 supercomputer at the University of Southampton.

References

Baker, C.J., 2014. A review of train aerodynamics Part 2 – applications. Aeronaut. J. 118 (1202), 345–382.
Bell, J.R., Burton, D., Thompson, M.C., Herbst, A.H., Sheridan, J., 2015. Moving model analysis of the slipstream and wake of a high-speed train. J. Wind Eng. Ind. Aerod. 136, 127–137.
Brun, C., Aubrun, S., Goossens, T., Ravier, P., 2008. Coherent structures and their frequency signature in the separated shear layer on the sides of a square cylinder. Flow, Turbul. Combust. 81 (1), 97–114.
Carley, M., 2011. Turbulence and Noise. https://people.bath.ac.uk/ensmjc/Notes/tnoise.pdf.
Chung, T.J., 2002. Computational Fluid Dynamics. Cambridge University Press, Cambridge.
Craft, T., Gant, S., Iacovides, H., Launder, B., 2004. A new wall function strategy for complex turbulent flows. Numer. Heat Tran., part B: fundamentals 45 (4), 301–318.
Craft, T.J., Gant, S., Gerasimov, A., Iacovides, H., Launder, B., 2006. Development and application of wall-function treatments for turbulent forced and mixed convection flows. Fluid Dynam. Res. 38 (2–3), 127.
Curle, N., 1955. The influence of solid boundaries upon aerodynamic sound. Proc. Roy. Soc. Lond. A 231 (1187), 505–514.
Dong, T., Liang, X., Krajnović, S., Xiong, X., Zhou, W., 2019. Effects of simplifying train bogies on surrounding flow and aerodynamic forces. J. Wind Eng. Ind. Aerod. 191, 170–182.
Eça, L., Saraiva, G., Vaz, G., Abreu, H., 2015. The Pros and Cons of Wall Functions.
Farassat, F., 2007. Derivation of Formulations 1 and 1A of Farassat.
Gao, G., Li, F., He, K., Wang, J., Zhang, J., Miao, X., 2019. Investigation of bogie positions on the aerodynamic drag and near wake structure of a high-speed train. J. Wind Eng. Ind. Aerod. 185, 41–53.
Guo, Z., Liu, T., Chen, Z., Xia, Y., Li, W., Li, L., 2020. Aerodynamic influences of bogie's geometric complexity on high-speed trains under crosswind. J. Wind Eng. Ind. Aerod. 196, 104053.
Guo, Z., Liu, T., Xia, Y., Liu, Z., 2022. Aerodynamic influence of the clearance under the cowcatcher of a high-speed train. J. Wind Eng. Ind. Aerod. 220, 104844.
Harwood, A.R.G., Dupère, I.D.J., 2016. Numerical evaluation of the compact acoustic Green's function for scattering problems. Appl. Math. Model. 40 (2), 795–814.
He, Y., 2023. PhD thesis. In: Aerodynamic Noise Simulation of High-Speed Train Bogie. University of Southampton.
He, Y., Thompson, D., Hu, Z., 2021. Numerical investigation of flow-induced noise around a high-speed train bogie in a simplified cavity. In: International Conference on Rail Transportation, pp. 65–72. Chengdu.
Jing, G., Ding, D., Liu, X., 2019. High-speed railway ballast flight mechanism analysis and risk management – a literature review. Construct. Build. Mater. 223, 629–642.
Kim, H., Hu, Z., Thompson, D., 2020. Numerical investigation of the effect of cavity flow on high speed train pantograph aerodynamic noise. J. Wind Eng. Ind. Aerod. 201, 104159.
Lan, J., Han, J., 2017. Research on the radiation characteristics of aerodynamic noises of a simplified bogie of the high-speed train. J. Vibroengineering 19 (3).
Latorre Iglesias, E., Thompson, D.J., Smith, M., Kitagawa, T., Yamazaki, N., 2017. Anechoic wind tunnel tests on high-speed train bogie aerodynamic noise. Int. J. Real. Ther. 5 (2), 87–109.
Lauterbach, A., Ehrenfried, K., Kröber, S., Ahlefeldt, T., Loose, S., 2010. Microphone Array Measurements on High-Speed Trains in Wind Tunnels. Berlin Beamforming Conference, Citeseer.
Lauterbach, A., Ehrenfried, K., Loose, S., Wagner, C., 2012. Microphone array wind tunnel measurements of Reynolds number effects in high-speed train aeroacoustics. Int. J. Aeroacoustics 11 (3–4), 411–446.
Li, T., Qin, D., Zhang, W., Zhang, J., 2020. Study on the aerodynamic noise characteristics of high-speed pantographs with different strip spacings. J. Wind Eng. Ind. Aerod. 202, 104191.
Liang, X.-f., Liu, H.-f., Dong, T.-y., Yang, Z.-g., Tan, X.-m., 2020. Aerodynamic noise characteristics of high-speed train foremost bogie section. J. Cent. S. Univ. 27 (6), 1802–1813.
Liu, X., Hu, Z., Thompson, D., Jurdic, V., 2018. Reduction of aerodynamic noise from square bars by introducing spanwise waviness. J. Sound Vib. 435, 323–349.
Liu, X., Thompson, D.J., Hu, Z., 2019. Numerical investigation of aerodynamic noise generated by circular cylinders in cross-flow at Reynolds numbers in the upper subcritical and critical regimes. Int. J. Aeroacoustics 18 (4–5), 470–495.
Liu, X., Zhang, J., Thompson, D.J., Latorre Iglesias, E., Squicciarini, G., Hu, Z., Toward, M., Lurcock, D., 2021. Aerodynamic noise of high-speed train pantographs: Comparisons between field measurements and an updated component-based prediction model. Appl. Acoust. 175, 107791.
Minelli, G., Yao, H.D., Andersson, N., Höstmad, P., Forssén, J., Krajnović, S., 2020. An aeroacoustic study of the flow surrounding the front of a simplified ICE3 high-speed train model. Appl. Acoust. 160, 107125.
Nagakura, K., 2006. Localization of aerodynamic noise sources of Shinkansen trains. J. Sound Vib. 293 (3), 547–556.
Oza, U., Hu, Z., Zhang, X., 2016. DDES Simulation of a Complex Main Landing Gear with Six-Wheel Bogie. 34th AIAA Applied Aerodynamics Conference.
Ricciardi, T.R., Wolf, W.R., Moffitt, N.J., Kreitzman, J.R., Bent, P., 2021. Numerical noise prediction and source identification of a realistic landing gear. J. Sound Vib. 496, 115933.
Ricco, P., Baron, A., Molteni, P., 2007. Nature of pressure waves induced by a high-speed train travelling through a tunnel. J. Wind Eng. Ind. Aerod. 95 (8), 781–808.
Sawamura, Y., Uda, T., Kitagawa, T., Yokoyama, H., Iida, A., 2021. Measurement and reduction of the aerodynamic bogie noise generated by high-speed trains. In: Degrande, G., Lombaert, G., Anderson, D., et al. (Eds.), Terms of Wind Tunnel Testing. Noise and Vibration Mitigation for Rail Transportation Systems;Noise and Vibration Mitigation for Rail Transportation Systems. Notes on Numerical Fluid Mechanics and Multidisciplinary Design, vol. 150. Springer International Publishing, Cham, pp. 73–80. https://doi.org/10.1007/1978-1003-1030-70289-70282_70285.
Shur, M., Spalart, P., Strelets, M., Travin, A., 1999. Detached-eddy simulation of an airfoil at high angle of attack. In: Proceedings of the 4th International Symposium on Engineering Turbulence Modelling and Measurements. Elsevier, Ajaccio, Corsica, France, pp. 669–678.
Sima, M., Gurr, A., Orellano, A., 2008. Validation of CFD for the flow under a train with 1: 7 scale wind tunnel measurements. In: Proceedings of the BBAA VI International Colloquium on Bluff Bodies Aerodynamics and Applications. Milano, Italy.
Spalart, P., Allmaras, S., 1992. A one-equation turbulence model for aerodynamic flows. 30th Aero. Sci. Meet. Exhib. 439.
Spalart, P.R., Deck, S., Shur, M.L., Squires, K.D., Strelets, M.K., Travin, A., 2006. A new version of detached-eddy simulation, resistant to ambiguous grid densities. Theor. Comput. Fluid Dynam. 20 (3), 181.
Spalart, P.R., Streett, C., 2001. Young-person's guide to detached-eddy simulation grids. No. NAS 1 (26), 211032.
Thompson, D.J., Latorre Iglesias, E., Liu, X., Zhu, J., Hu, Z., 2015. Recent developments in the prediction and control of aerodynamic noise from high-speed trains. Int. J. Real. Ther. 3 (3), 119–150.
Tian, H., 2019. Review of research on high-speed railway aerodynamics in China. Transport. Saf. Environ. 1 (1).
Vuillot, F., Lupoglazoff, N., Luquent, D., Sanders, L., Manoha, E., Redonnet, S., 2012. Hybrid CAA solutions for nose landing gear noise. In: 18th AIAA/CEAS Aeroacoustics Conference (33rd AIAA Aeroacoustics Conference).
Wang, M., Freund, J.B., Lele, S.K., 2005. " Computational prediction of flow-generated sound ". Annu. Rev. Fluid Mech. 38 (1), 483–512.
Wang, Y., Thompson, D., Hu, Z., 2019. Effect of wall proximity on the flow over a cube and the implications for the noise emitted. Phys. Fluid. 31 (7), 077101.
Yamazaki, N., Uda, T., Kitagawa, T., Wakabayashi, Y., 2019. Influence of bogie components on aerodynamic bogie noise generated from shinkansen trains. Q. Rep. RTRI 60 (3), 202–207.
Zhang, J., Wang, J., Wang, Q., Xiong, X., Gao, G., 2018. A study of the influence of bogie cut outs' angles on the aerodynamic performance of a high-speed train. J. Wind Eng. Ind. Aerod. 175, 153–168.
Zhu, C., Hemida, H., Flynn, D., Baker, C., Liang, X., Zhou, D., 2017. Numerical simulation of the slipstream and aeroacoustic field around a high-speed train. Proc. Inst. Mech. Eng. F J. Rail Rapid Transit 231 (6), 740–756.
Zhu, J., Hu, Z., Thompson, D., 2014. Flow simulation and aerodynamic noise prediction for a high-speed train wheelset. Int. J. Aeroacoustics 13 (7–8), 533–552.
Zhu, J., Hu, Z., Thompson, D., 2017. The effect of a moving ground on the flow and aerodynamic noise behaviour of a simplified high-speed train bogie. Int. J. Real. Ther. 5 (2), 110–125.
Zhu, J., Hu, Z., Thompson, D., 2018. The flow and flow-induced noise behaviour of a simplified high-speed train bogie in the cavity with and without a fairing. Proc. Inst. Mech. Eng. F J. Rail Rapid Transit 232 (3), 759–773.
Zhu, J., Hu, Z., Thompson, D.J., 2016. Flow behaviour and aeroacoustic characteristics of a simplified high-speed train bogie. Proc. Inst. Mech. Eng. F J. Rail Rapid Transit 230 (7), 1642–1658.